Fe_5S_2 identified as a host of sulfur in Earth and planetary cores

Claire C. Zurkowski[a †], Barbara Lavina[b,c], Abigail Case[a], Kellie Swadba[a], Stella Chariton[b], Vitali Prakapenka[b], Andrew J. Campbell[a]

[a]University of Chicago, Department of the Geophysical Sciences, 5734 S Ellis Ave, Chicago, IL 60637, USA
[b]Center for Advanced Radiation Sources, 9700 South Cass Avenue, Building 434A, Argonne, IL 60439, USA
[c]X-ray Science Division, Advanced Photon Source, Argonne National Laboratory, Argonne, IL 60439, USA
[†]Now at Earth and Planets Laboratory, Carnegie Institution for Science, 5251 Broad Branch Road, NW, Washington, DC 20015, USA

Corresponding Author: Claire Zurkowski, czurkowski@carnegiescience.edu

ABSTRACT

Cosmochemical considerations suggest that sulfur is a candidate light alloying element in rocky planetary cores, such that the high pressure-temperature (*P*-*T*) Fe-S phase relations likely play a key role in planetary core crystallization thermodynamics. The iron-saturated Fe-S phase relations were investigated to 200 GPa and 3250 K using combined powder and single-crystal X-ray diffraction techniques in a laser-heated diamond anvil cell. Upon heating at 120 GPa, *I*-4 Fe_3S is observed to break down to form iron and a novel hexagonal Fe_5S_2 sulfide with the Ni_5As_2 structure ($P6_3cm$, $Z = 6$). To 200 GPa, Fe_5S_2 and Fe are observed to coexist at high temperatures while Fe_2S polymorphs are identified with Fe at lower temperatures. An updated Fe-rich Fe-S phase diagram is presented. As this hexagonal Fe_5S_2 expresses complex Fe-Fe coordination and atomic positional disorder, crystallization of Fe_5S_2 may contribute to intricate elastic and electrical properties in Earth and planetary cores as they crystallize over time. Models of a fully crystallized Fe-rich Fe-S liquid in Earth's and Venus' core establish that Fe_5S_2 is likely the only sulfide to crystallize and may deposit in the outer third of the planets' cores as they cool. Fe_5S_2

could further serve as a host for Ni and Si as has been observed in the related meteoritic phase perryite, $(Fe, Ni)_8(P, Si)_3$, adding intricacies to elemental partitioning during core crystallization. The stability of Fe_5S_2 presented here is key to understanding the role of sulfur in the crystallization sequences that drive the geodynamics and dictate the structures of Earth and rocky planetary cores.

1. INTRODUCTION

Earth and terrestrial planets are composed of silicate mantles and iron-rich metallic cores (e.g. Birch 1952; McDonough and Sun 1995). Earth's core comprises a convecting liquid metal outer core and an actively crystallizing, denser inner core (Birch 1952; Dziewonski and Anderson 1981; Fearn and Loper, 1981). The seismically determined 3-8% density deficit in Earth's core compared to pure iron is thought to be accounted for by cosmochemically abundant light alloying elements, such as Si, O, S, C, and H (Masters and Gubbins, 2003; Irving et al. 2018; Kuwayami et al. 2020; McDonough 2003). The light element component of the metal core introduces complex *P-T*-dependent melting and crystallization thermodynamics and helps drive core convection as the planet cools over time (Fearn and Loper, 1981; Stevenson 1981; 1988; Nimmo 2015).

While there remains no method to directly sample Earth's or any terrestrial planetary core, iron meteorites are recognized as core relics of disrupted planetesimals, and have long provided insights into the light elements that sequester into the metallic component of planetary interiors (e.g. Scott and Wasson 1975; Malvin et al. 1984). Of the candidate core-alloying elements, sulfur is present in nearly all iron meteorites, suggesting that sulfur is a core alloying element in rocky planets of varying sizes, oxidation states, and formation histories (Scott and

53 Wasson 1975; Jones and Drake, 1983; Kruijer et al. 2014). Sulfur easily alloys with iron to high
54 pressures and temperatures, it is depleted in the silicate mantle compared to chondrites, and it
55 lowers the melting temperature of pure iron (e.g. Evans 1970; Fei 1995; McDonough and Sun
56 1995; Fei et al. 1997; Ozawa et al. 2013; Tateno et al. 2019). It follows that during the high
57 energy impact conditions of the late stage proto-Earth formation, sulfur would have facilitated
58 metal melt formation and density driven core segregation (Ringwood 1966; Murthy and Hall
59 1970; Shannon and Agee, 1996; Stevenson, 1988; Yoshino et al., 2003). Examination of the
60 structural properties of iron sulfides at high *P*-*T* is therefore fundamental to characterizing the
61 chemistry and thermodynamics of Earth and planetary cores.
62 The Fe-S phase relations are sensitive to *P*-*T*-composition conditions, and numerous Fe-
63 rich sulfide compounds have been observed: FeS, Fe_3S_2, Fe_2S, and Fe_3S (Evans 1970; King and
64 Prewitt 1982; Fei et al. 1995; Fei et al. 1997; Fei et al. 2000; Koch-Müller et al. 2002; Kamada et
65 al. 2010; Ozawa et al. 2013; Mori et al. 2017; Tateno et al. 2019). Fe_3S is reported to be the
66 stable Fe-rich sulfide between 21 and 250 GPa (Fei et al. 2000; Kamada et al. 2010; Ozawa et al.
67 2013), making it relevant at Earth's outer core conditions. Single crystal analysis of recovered
68 Fe_3S from 21 GPa establishes that it adopts a Fe_3P-type structure (*I*-4, *Z*=8) (Fei et al. 2000), and
69 no structural transitions have been reported in Fe_3S to 250 GPa (Ozawa et al. 2013; Kamada et
70 al. 2010; Thompson et al. 2020; Seagle et al. 2006; Morard et al. 2008; Mori et al. 2017). Above
71 ~250 GPa, Fe_3S breaks down at low temperatures into a *B*2 FeS + Fe phase assemblage, and
72 FeS+Fe reacts at high temperatures to form *C*37 Fe_2S + Fe at 306 GPa (Ozawa et al. 2013; Mori
73 et al. 2017; Tateno et al. 2019).
74 Although tetragonal Fe_3S has been reported to be stable to pressures encompassing
75 Earth's upper-to-mid-outer core, crystal structure analysis of Fe_3S has not been conducted at

Earth's core pressures, and unit-cell parameters for Fe_3S have only been reported up to 120 GPa at high temperatures (Seagle et al. 2006; Morard et al. 2008; Thompson et al. 2020). In the current study, Fe-rich Fe-S compositions were probed between 120 and 200 GPa using combined single-crystal and powder X-ray diffraction techniques. A novel hexagonal Fe_5S_2 sulfide (Ni_5As_2-type, $P6_3cm$, $Z = 6$) was identified co-crystallizing with Fe at high temperatures in this pressure range. Details of this complex hexagonal Fe_5S_2 structure along with the Fe_3S and Fe_2S structures observed at lower *P-T* are presented, and the Fe-rich Fe-S phase diagram is updated at Earth's outer core conditions. Results from this work reveal that Fe_5S_2 will eventually crystallize over a significant depth range in Earth's core, initiating at depths corresponding to ~240 GPa and depositing to the core-mantle boundary, as our planet cools overtime.

2. MATERIALS AND METHODS

Experiments targeting multigrain synthesis in the Fe-S system consisted of mixtures of Fe (99.9+%, <10μm, Alfa Aesar) and iron sulfide (FeS, 99.99%, Alfa Aesar). Two compositions were used in this study: Fe+12.5 wt% S ($Fe_{80}S_{20}$ molar proportions) and Fe + 23 wt% S ($Fe_{67}S_{33}$ molar proportions). The Fe-FeS compositions were ground in ethanol in a pestle and mortar for 1 hour then mixed dry for a short interval to homogenize any density settling during alcohol evaporation.

Pressure was generated using BX-90-type (Kantor et al. 2012) diamond anvil cells (DAC) with type 1 Boehler-Almax conical diamonds and seats, and Mao symmetric-type DACs with Type 1 standard cut diamonds mounted on tungsten carbide or cubic-boron nitride (cBN) seats. Diamond culets ranged from 150-50 μm in diameter. Foils of $Fe_{80}S_{20}$ or $Fe_{67}S_{33}$ were produced by pressing the Fe–S starting powders between two ungasketed diamond anvils, then loaded

between pellets of KCl or SiO_2. Sample chambers ranged from ~~1~~80-25 μm in diameter and were drilled from pre-indented rhenium gaskets. Samples were dried at 100º C for 30 minutes prior to pressurization.

Angle dispersive X-ray diffraction (XRD) experiments were conducted at Argonne National Laboratory, Sector 13 ID-D, of the Advanced Photon Source. At Sector 13 ID-D, a 2.5 μm x 3.54 μm full width, half maximum (FWHM) monochromatic X-ray beam tuned to 37 or 42 keV was utilized, and diffracted X-rays were collected with a CdTe 1M Pilatus detector. The detector was calibrated with LaB_6 NIST standard and single-crystal enstatite.

Double-sided laser heating and *in-situ* XRD collection took place at Sector 13 ID-D. Fiber lasers shaped with ~10 μm radius flat tops were aligned with the X-ray beam using the X-ray fluorescence of the sample pressure media or the gasket (Prakapenka et al., 2008). During heating, thermal emission from a 6 μm central region of the laser-heated spot was measured spectroradiometrically and fit to a gray body approximation (Heinz and Jeanloz, 1987). A 3% temperature correction was then applied to correct for axial gradients through the sample (Campbell et al., 2007; 2009). The laser power on each side of the sample was adjusted to maintain uniform double-sided heating and X-ray diffraction and temperature measurements were collected every ~200 K with 1s exposure times. Samples were typically quenched at high temperatures within 30-45 minutes of heating or after a phase transition and suitable grain growth was observed. Powder diffraction patterns were processed using Dioptas (Prescher and Prakapenka, 2015) and CrysalisPro (Rigaku OD, 2018). Pressure was determined using the equation of state of hcp-Fe (Dewaele et al. 2006).

Upon quenching, X-ray diffraction maps of the heated spot were collected across a 100 μm^2 square region in 3 μm steps. Map locations showing high intensity, spotty diffraction

patterns were chosen for multigrain single-crystal type X-ray diffraction collection approach, as these features indicate high-temperature induced crystallite growth. At chosen map locations, X-ray diffraction images were collected across ±17 to ±30º rotational scans in 0.25º–0.5º steps with 1– 4 s exposure times. The diffraction reflections were then mapped in the reciprocal space and target grains were identified and separated from reflections associated with the pressure media, iron, and diamond (Rigaku OD, 2018).

Iron-sulfide lattices were then indexed and the peak intensities were integrated and reduced using CrysalisPro (Rigaku OD, 2018). Known structure models (El-Boragy et al. 1970; Oryshchyn et al. 2011) were refined to the reduced structure factors and lattice geometries using SHELXL2014/7 (Sheldrick 2015). A few reflections showing outlying calculated versus measured structure factors; likely due to overlap with diamond and other phases in the multigrain sample, resolution limitations, and volume of crystal illuminated by the X-ray beam, were omitted. The refinement statistics and crystallographic information files (CIFs) for each structure model presented can be found in the supplemental information and appendices.

3. RESULTS

3.1 Synthesis and identification of Fe_5S_2 to 200 GPa

Upon compression between 119(2) and 193(4) GPa and after heating to temperatures between 2400–3300 K, the diffraction patterns are characterized by recrystallized hcp-Fe and diffuse streaks and sets of closely spaced Bragg peaks suggestive of a complex atomic arrangement of the coexisting sulfide (Figure 1, S1). With sustained heating, large sulfide grain growth (3 – 6 μm) is observed (Figure 1). The diffraction angles for this synthesized sulfide phase are not compatible with the Fe_3P-type Fe_3S at these conditions (Kamada et al., 2014). Recrystallization of hcp-Fe at high temperatures was observed in all experiments using the

145 $Fe_{80}S_{20}$ and $Fe_{67}S_{33}$ starting powders as evidenced by the spotty (100) and (101) hcp-Fe rings in
146 Figure 1a. Fe recrystallization with this high-temperature Fe-sulfide establishes that the probed
147 sample locations were in a Fe-saturated phase field (Figure 1a) and this sulfide phase is
148 important to consider further in the context of Fe-rich planetary cores.

149 Upon temperature quenching in this pressure range, diffraction images were collected
150 while rotating the DAC across a +/- 17–30º range (depending on the DAC opening). Grains of a
151 hexagonal lattice were identified in the reciprocal space with indexed parameters: a = 5.979(3)
152 Å, c = 11.088(6) Å at 140(2) GPa and 3070(180) K (Figure 1b, Table 1). However, across the *P*-
153 *T* explored, three polytypes of this phase were observed (Table 1). Each indexed grain exhibits
154 an a axial length of ~ 6 Å, while 3 differing c axial lengths are identified: ~ 11, 26, and 73 Å.
155 Diffraction mappings show that the polytypism is accompanied by diffuse scattering along the c
156 direction suggesting positional disorder along this axis (Figure S1). Decreased diffuse scattering
157 is observed after continued heating at peak temperatures in the KCl pressure media, and grains
158 with a ~ 6 Å, c ~ 11 Å were indexed (Figure 1b). This unit cell likely represents the most
159 positionally ordered arrangement relevant at these high *P*-*T* conditions.

160 The crystal structure of the Fe-sulfide synthesized at 140(2) GPa and 3070(180) K was
161 determined based on 159 observed reflections at these extreme conditions (Table S1).
162 Assessment of the systematic absences for the reduced structure factors suggests a $P6_3cm$ space
163 group, and structural solution and positional and displacement parameter refinement converged
164 on a Fe_5S_2 compound adopting the Ni_5As_2 structure type (Table S1, 3; Figure 2) (Oryshchyn et
165 al. 2011). The measured unit cell parameters for this polytype are compatible with 6 formula
166 units per cell volume of Fe_5S_2. Furthermore, analogous polytypism due to stacking variations
167 along the c direction have been observed in related transition metal binary phases such as Pb_5As_2

(Saini et al. 1964). The diffraction angles and intensities measured in this study cannot be modeled based on the tetragonal Fe_3S structure previously reported at these conditions (Kamada et al., 2012; Ozawa et al., 2013; Mori et al., 2017).

The Ni_5As_2 structure that Fe_5S_2 adopts is a slight modification of the Pb_5Sb_2 structure (El-Boragy et al. 1970), where the *M*6 site (*M* = metal) (Table 2) is split about its position and given half occupancy, resulting in a change in Wyckoff site from 6c to 12d (Figure 2) (Oryshchyn et al. 2011). A significant improvement to the Fe_5S_2 refinement statistics was observed when incorporating the disordered Fe6 site, suggesting that the Ni_5As_2 structure model better describes the Fe_5S_2 structure factors (Table S1). Displacement parameters for the Fe_5S_2 structure model were refined as isotropic. Displacement parameters showing errors > 3$\boldsymbol{\sigma}$ were fixed to a value equal to the average displacement parameter value for Fe or S sites (Table 2). The isotropic displacement parameter for the disordered Fe site was also fixed at an average Fe_{Uiso} value (Table 2). The number of reflections collected at these extreme pressures limits the number of statistically meaningful parameters to refine, and fixing displacement parameters to reasonable values precludes overinterpretation of the current dataset.

A CIF file for the final Fe_5S_2 structure model is provided in Appendix A1. Following previous descriptions of related M_5X_2 phases (e.g. Kjekshus et al. 1973; Oryshchyn et al. 2011), Fe_5S_2 can be viewed as an arrangement of 6 Fe sites and 3 S sites with the Fe1, Fe2, Fe4, and Fe6 sites in 13-fold coordination, the Fe3 and Fe5 sites in 12-fold coordination, and the S sites in 10-fold coordination (Figure 2c, Table 3). All sites are coordinated by both Fe and S sites. Average Fe-Fe and Fe-S bond lengths, more generally, are not well established at these high *P*-*T* conditions, and this description of Fe and S coordination serves to confirm that our observations are compatible with analogue M_5X_2 phases (e.g. Kjekshus et al. 1973; Oryshchyn et al. 2011).

The range of interatomic distances measured in Fe_5S_2 at 140 GPa are given in Table 3 and Figure S2. The shortest Fe-Fe distance observed is 2.14(2) Å (Table 3).

Final R_1 values ≃ 10% attest to the less-than ideal quality of the multigrain dataset as a possible result of the 1-2 megabar synthesis conditions and observed *c* axial disorder and stacking complexities in Fe_5S_2 (Table S1). Previous studies of isomorphic Ni_5As_2 and related Pb_5As_2 at ambient conditions have also reported similar quality of refinements despite obtaining significantly more reflections from ambient samples (e.g. Saini et al. 1964; El-Boragy et al. 1970; Kjekshus et al. 1973). Notable challenges regarding the refinement of the Fe_5S_2 structure model at these extreme conditions are discussed here and compared with similar difficulties reported in previous characterizations of this structure type.

Thirteen violations of the $P6_3cm$ systematic absence condition: $l = 2n + 1$ for $(0kl)$, were flagged during the refinement of Fe_5S_2. The reflections associated with these systematic absence violations were examined in the raw diffraction images and show low, diffuse intensity. Discrepancy over the presence or absence of weak reflections with $(0kl)$, l=2n has been reported in previous investigations of Ni_5As_2 and Pb_5As_2 (e.g. Saini et al. 1964; El-Boragy et al. 1970; Kjekshus et al. 1973), suggesting that these studies also faced difficulties with space-group determination. Observations of these low-intensity reflections could be a result of residual disorder along the *c* direction, and longer heating cycles may be required for the atoms to arrange into equilibrium positions. It is likewise possible that differing synthesis methods for Ni_5As_2 and Pb_5As_2 in previous ambient condition studies resulted in the formation of varying polytypes. Ni_5As_2 and isomorphic Ni_5P_2 also exhibits a homogeneity range of ~71.25 – 72.7 atomic % nickel (Kjekshus et al. 1973; Litasov et al., 2019). Additionally, slight stacking modifications of the M_5X_2 structures are observed in trigonal structures such as $Ni_{31}Si_{12}$ (Frank and Schubert

1971) and $(Fe, Ni)_8(Si, P)_3$ (perryite) (Okada et al. 1991). Attempts to refine the current Fe-sulfide phase with the $Ni_{31}Si_{12}$ or perryite structure models did not significantly improve the refinement statistics as the current high *P-T* dataset is too limited to resolve the intricacies that differentiate these structures. Based on the presence of disorder, polytypism, anisotropic vibrational motion, and nonstoichiometry in the related M_5X_2 phases, additional nuances to the Fe_5S_2 structure model may be developed in future studies; however, the identification and characterization of the Fe_5S_2 crystal structure determined here to 200 GPa is novel, and the observations and challenges reported in this study align with that of previous analyses of Ni_5As_2 and Pb_5Sb_2 that were not affected by the limitations associated with performing microdiffraction in a DAC at extreme conditions.

3.2 Other sulfides observed during heating to 200 GPa and comparison of their structures with Fe_5S_2

X-ray diffraction from seven heating cycles performed between 100 and 200 GPa and to 3300 K provide insight into the Fe-rich Fe-S phase relations at outer core pressures and to high temperatures. In each heating experiment, temperatures near melting were attained, and lattices of Fe_5S_2 were indexed in the reciprocal space upon quenching. By further probing locations across the thermal gradient of the laser heated spots, additional Fe-sulfides were characterized, offering information on the lower temperature Fe-saturated sulfide crystal chemistries (Table 1, S1). These include Fe_3P-type Fe_3S (*I*-4, *Z* = 8), *C*23 Fe_2S (Co_2P-type, *Pnma*, *Z* = 4), and *C*37 Fe_2S (Co_2Si-type, *Pnma, Z*=4), in lower temperature regions at 119 GPa, 131 GPa, and 140 GPa, respectively (Figure 3; Table 1, S1).

Grains of tetragonal Fe_3S (*I*-4, *Z* = 8) (referred to herein as *I*-4 Fe_3S) were indexed with parameters: *a* = 8.094(3) Å, *c* = 3.990(2) Å at 119(2) GPa, and refined to the Fe_3P-type structure model (*I*-4, *Z* = 8) (referred to herein as *I*-4 Fe_3S), in agreement with previous studies (Fei et al. 2000; Seagle et al. 2006; Morard et al. 2007; Kamada et al. 2010; Kamada et al. 2012; Thompson et al. 2020) (Table S1, Figure 3a, Appendix A2). The structure can be viewed as containing 3 tetrahedrally coordinated Fe sites (Blanchard et al. 2008): one Fe-site is coordinated only by S atoms with an average bond length of 2.083(9) Å, another Fe site is coordinated by 3 S atoms and 1 Fe atom with an average bond length of 2.146(8) Å, and the third Fe site is coordinated by 2 S and 2 Fe atoms with an average bond length of 2.137(8) Å (Figure 3; Table S2). The shortest Fe-Fe distance measured in Fe_3S at 120 GPa is 2.160(8) Å, while the shortest Fe-Fe distance calculated for Fe_3S at ambient conditions is 2.36 Å (Fei et al., 2000). This comparison indicates ~ 10% contraction of Fe-Fe bond lengths in Fe_3S across this pressure range. This value is also similar to the shortest Fe-Fe distance measured in Fe_5S_2 at 140 GPa (Table 3).

After heating at 131(2) GPa, grains of Fe_3S were not observed across the heated spot. Instead, orthorhombic lattices were also identified with parameters *a* = 4.869(2) Å, *b* = 3.256(2) Å, *c* = 6.139(2) Å, compatible with 4 formula units of Fe_2S. Structural solution and refinement indicate that the Fe_2S grains adopt the *C*23 structure (Co_2P type, *Pnma*, *Z* = 4) in agreement with previous structural analyses at lower pressures (Zurkowski et al. 2022) (Table S1, Figure 3b, Appendix A3). The structure can be viewed as composed of columns of FeS_4 tetrahedra and columns of FeS_5 square pyramids linked along edges in the *b* direction (Figure 3b). The average Fe–S bond lengths are 2.213(8) Å and 2.011(2) Å in the square pyramids and tetrahedra, respectively (Table S3). These values are comparable with those observed in *C*23 Fe_2S at 90 GPa

(Zurkowski et al. 2022), and show up to ~3% compression of Fe-S bond lengths between 90 and 130 GPa.

Upon temperature quenching at 140(2) GPa, orthorhombic grains were identified in the sample chamber with a = 4.667(2) Å, 3.289(1) Å, 6.186(4) Å. This unit cell is similar to the *C*23 Fe_2S cell measured at 130 GPa, but it exhibits a 4 % contraction of the *a* axial length, a 1% extension of the *b* and *c* axial lengths, and a 2% volume decrease. Structure solution and refinement establishes that Fe_2S adopts the *C*37 structure (Co_2Si-type, *Pnma, Z*=4) (Table S1, Figure 3c, Appendix A4). This result confirms the previously proposed *C*23–*C*37 transition in Fe_2S at these conditions and presents a comparable volume change (Zurkowski et al., *in press*). Inherent to the *C*23–*C*37 transition is coordination change from the 4-fold Fe1 coordination polyhedra in the *C*23 structure to the 5-fold dipyramid polyhedra in the *C*37 structure (Figure 3b, c). Comparing the *C*23 and *C*37 structure models determined at 130 and 140 GPa, respectively, a 10% contraction of the Fe – S interatomic distance associated with this coordination change is observed across the transition (Figure S2; Table S3). The average Fe–S bond lengths measured in *C*37 Fe_2S are 2.196(2) Å and 2.165(3) Å in the square pyramids and dipyramids, respectively (Table S4). These values are comparable with those observed in *C*23 Fe_2S in this study and the overall increase in average interatomic distances in one of the polyhedra is associated with the increase in coordination.

Comparison of the interatomic distances and coordination environments in the Fe-sulfides observed in this study distinguishes Fe_5S_2 as particularly unique among them. Fe-Fe bond distances at multi-megabar pressures are not well known. For comparison of the possible coordination environments of the iron-sulfides discussed here, we estimated a maximum Fe-Fe bond length of ~2.3 Å based on a linear extrapolation of Fe-Fe distances with pressure from

Ishimatsu et al., (2021) and the compression of Fe-Fe distances in Fe_3S at these conditions compared to ambient pressures (Fei et al., 2021). Within an interatomic distance of ~2.3 Å (Table 3, Appendix A1-A4), *C*23 and *C*37 Fe_2S consist of Fe sites coordinated only by S (Table S3, S4), Fe_3S exhibits up to 3 Fe-Fe bonds (Table S2), and Fe_5S_2 exhibits up to 5 Fe-Fe bonds (Table 3) Even though Fe_5S_2 is more S-rich than Fe_3S by ~3 wt%, Fe_5S_2 has significantly increased Fe-Fe coordination. It follows that increased metallic interactions would be associated with the stability of Fe_5S_2 at Earth and planetary core conditions (Figure 2c; S2, Table 3; S2).

3.3 Fe-rich sulfide phase relations at core-mantle boundary pressures

The presented single-crystal derived structures of Fe_5S_2, Fe_3S, *C*23 Fe_2S and *C*37 Fe_2S were then used to inform the changes in diffraction patterns collected during heating between 110 and 200 GPa and to ~3250 K (Figure 4). Beginning at 112 GPa, diffraction signal from *C*23 Fe_2S coexisting with Fe was first identified upon heating of the $Fe_{80}S_{20}$ starting material to ~2000 K (Figure 4). With continued heating, peaks associated with tetragonal Fe_3S were observed over a limited temperature range ($\lesssim$ 2400 K) until streaks of diffuse scattering signal and Bragg reflections from Fe_5S_2 first appeared. Crystallization of the Fe_5S_2 and hcp-Fe occurred with continued heating to 119(2) GPa and 2840(180) K (Figure 4).

Upon heating beginning at 120 GPa, *C*23 Fe_2S was observed coexisting with Fe to 122(1) GPa and 2290(120) K, above which diffraction from the Fe_5S_2 phase was identified and Fe_5S_2 crystallites formed coexisting with hcp-Fe to 131(2) GPa and 3050(140) K (Figure 4). *I*-4 Fe_3S was not observed. With continued heating cycles between 133(1) GPa and 194(2) GPa and up to 3250 K in the $Fe_{80}S_{20}$ composition, *C*37 Fe_2S coexists with Fe at moderate temperatures and a reaction to form Fe_5S_2 occurs at high temperatures (Figure 4). A pressure-induced *C*23–*C*37 Fe_2S

transition is therefore constrained between 125 and 135 GPa, in agreement with previous investigations of Fe_2S (Zurkowski et al. *in press*). In the heating cycle conducted on the $Fe_{67}S_{33}$ composition at ~145 GPa, compatible phase relationships are observed (Figure 4), suggesting that the probed location of the sample was Fe-rich.

The stability of Fe_5S_2 coexisting with Fe between 120 and 200 GPa and to 3250 K ~~also~~ requires a change in melting behavior associated with the change in solidus phase from *I*-4 Fe_3S to Fe_5S_2 above 120 GPa. As Fe_5S_2 is observed to temperatures of ~3250 K, a kink in the Fe-sulfide solidus curve (Mori et al. 2017) is proposed to accommodate this transition (Figure 4). Further work examining the onset of melting under these conditions will be helpful for accurately determining the shape of the solidus curve above 120 GPa.

The resultant phase diagram shown in Figure 4 estimates the phase boundaries for the stable sulfide coexisting with iron between ~100 – 200 GPa. As previous chemical analyses studies have reported approximately 3.5 wt% S dissolved in hcp-Fe with no clear pressure dependence between 75 and 250 GPa (Kamada et al., 2010; 2012; Mori et al., 2017), we can expect that this phase diagram is relevant to compositions ranging from Fe—3.5 wt % S (minimum sulfur content required to crystallize a sulfide) to Fe—16 wt % S (composition of Fe_3S). For compositions in the 16 – 19 wt % S range, between Fe_3S and Fe_5S_2, iron would no longer crystallize in the Fe_3S stability field (<120 GPa, high temperatures), and for compositions between in the 19 – 22 wt % S range, between Fe_5S_2 and Fe_2S, iron would no longer crystallize in the Fe_3S or Fe_5S_2 stability fields (up to 200 GPa, high temperatures).

4. DISCUSSION

4.1 Discrepancies among the current and previous studies

Transitional metal binary compounds with metal-to-nonmetal ratios ranging from 2.33–2.66 (~70–73 atm% metal) predominantly adopt complex trigonal or hexagonal structures with considerable metal-metal bonding (Chen and Whitmire 2018 and references therein). Our observations of the disorder, polytypism, and complex coordination environments inherent to Fe_5S_2 demonstrate that it aligns with this systematic characterization. Interestingly, this work elucidates that the Fe_5S_2 atomic arrangement is thermodynamically favored and expresses greater Fe-Fe interactions at the extreme conditions of Earth's outer core compared to that of *I*-4 Fe_3S.

These results are contrary to previous reports of Fe_3S stability ~~on~~ to high temperatures in Fe-rich systems to 250 GPa (Kamada et al. 2010; Kamada et al. 2012; Ozawa et al. 2013; Mori et al. 2017), but our observations may account for these discrepancies. First, interpretation of Fe_5S_2 in the integrated powder diffraction patterns is difficult due to the variation in diffraction signal obtained from the Fe_5S_2 polytypes and the low intensity scattering from the disordered sites during its formation (Figure S1, S4). Fe_5S_2 also forms large crystallites rather than a fine-grain powder, limiting the diffraction peaks observed at one orientation and rendering accurate indexation of Fe_5S_2 quite challenging without rotating the sample (Figure 1a). The implementation of single-crystal X-ray diffraction techniques at high pressures was critical in the current study to accurately characterize the hexagonal unit cell geometry and complex structure of the Ni_5As_2-like Fe_5S_2 and to constrain the stability field of *I*-4 Fe_3S.

Several studies have also reported chemical analysis of Fe_3S grains in samples recovered from high temperatures in the 200–250 GPa range (Mori et al. 2017; Yokoo et al. 2019; Ozawa et al. 2013), but the difference in Fe content between Fe_3S and Fe_5S_2 may be as small as 2.3%

when accounting for ~71.25 – 72.7 atm % metal stoichiometry range of related M_5X_2 phases (Kjekshus et al. 1973; Litasov et al., 2019). This value is generally within 3σ uncertainty reported for chemical analyses of samples recovered from these extreme conditions, posing another challenge for distinguishing between the synthesis of Fe_3S and Fe_5S_2. TEM analysis of a Fe–S sample recovered from 236 GPa and 2980 K reveals sulfide grains with on average ~73 atm% Fe (Ozawa et al. 2013); this value is within 0.3–1.25 atom % of the possible range of Fe_5S_2 stoichiometries and 2 atomic percent less than an Fe_3S composition. The results from previous chemical analyses of samples recovered from outer core pressures and high temperatures (Mori et al. 2017; Yokoo et al. 2019; Ozawa et al. 2013) therefore do not contradict the current results, and simply indicate previous misinterpretation of Fe_5S_2 as Fe_3S, based on EDS measurements alone and in the absence of single-crystal diffraction analysis. Additionally, as previous analyses of S-solution in hcp-Fe indicate ~3.5 wt% S in iron metal between ~75 – 250 GPa (Kamada et al., 2010; 2012; Mori et al., 2017), one can expect that iron is also saturated with this amount of sulfur in the present work, which was conducted in a similar compositional range. This supports that the pressure-temperature stability fields of Fe_3S and Fe_5S_2 would not differ due to stoichiometric effects between this study and previous Fe-rich Fe-S studies (e.g., Mori et al., 2017; Kamada et al, 2010; 2012; Ozawa et al., 2013).

4.2 Sulfur in Earth and Planetary cores

The stability of Fe_5S_2 and the phase relations observed in this study present novel constraints on the material properties of Fe-sulfides at conditions relevant to Earth's outer core, Venus' core, and exoplanetary cores of similar size and core-mass fraction (CMF). Namely, at pressures ≥120 GPa, Ni_5As_2-type Fe_5S_2, not tetragonal Fe_3S as previously believed (e.g. Kamada

et al., 2010; Ozawa et al., 2013; Mori et al., 2017; Tateno et al., 2019), is the relevant Fe-rich sulfide. As Earth's outer core crystallizes over time, Fe_5S_2 may eventually crystallize over a large depth range up to the CMB.

To test this, the crystallization of an Fe-S liquid in Earth's core was modeled for bulk starting sulfur contents of < 4 wt% (Figure 5a), based on cosmochemical approximations (McDonough and Sun 1995), metal-silicate partitioning studies (Suer et al., 2018), and the requisite to crystallize an Fe-rich inner core (Mori et al., 2017). These values, however, do not account for Earth's core density deficit (Dziewonski and Anderson, 1981; Irving et al., 2018), and additional light elements such as Si, O, C and H are understood to be present to some degree (McDonough and Sun 1995). As sulfur is known to significantly lower the melting temperature of Fe (e.g. Campbell et al., 2007; Mori et al., 2017; Kamada et al., 2012), the crystallization of other light-element rich phases in a multicomponent systems will likely occur prior to Fe-sulfide crystallization, further saturate the remaining liquid in sulfur, and induce sulfide crystallization at greater depths. This model therefore represents the minimum depth at which Fe-sulfide crystallization can be expected in Earth's core (Figure 5a).

The model begins with a fully molten Fe-S core and bulk core sulfur contents ranging from 1 – 4 wt %. Equations of state of hcp-Fe (Dewaele et al., 2006) and Fe_2S (Zurkowski et al., *in press*) were then used to determine the density of Fe and S at these conditions and convert these values to volume percent. For each shell of Fe crystallization starting from the center of the planet, the liquid outer core sulfur concentration becomes increasingly S-rich, and the pressure at which the sulfur concentration of the outer core liquid becomes S-rich of the projected Fe-S eutectic (Mori et al., 2017) marks the onset of Fe + Fe-sulfide crystallization. The results of this calculation are shown in Figure 5a. For the range of 1 – 4 wt % sulfur in the bulk core, the onset

of Fe + sulfide crystallization can be expected between 150 and 240 GPa, respectively. This range of pressures encompasses the conditions where Fe + Fe_5S_2 are observed in the current study, while *C*37 Fe_2S + Fe is identified above 250 GPa (Tateno et al., 2019). These results suggest that Fe + Fe_5S_2 deposition is likely to initiate at pressures < 240 GPa, ~ 4000 km depth (Dziewonski and Anderson, 1981), and continue to the core-mantle boundary (Figure 5a). While future studies may better constrain the Fe + Fe_5S_2 → Fe + Fe_2S boundary, Fe_2S is not likely to crystallize in Earth's core, as the outer core liquid is not sufficiently S-rich at these pressures, based on the current calculation.

In this study, tetragonal Fe_3S has been confirmed to 120 GPa in agreement with previous studies (Figure 4) (Seagle et al. 2006; Morard et al. 2008; Thompson et al., 2020). Rocky planetary bodies with sizes and CMFs like that of Venus (CMB = 114 GPa, central pressure = 274 GPa) (Aitta 2012) would likely crystallize out Fe_3S and Fe_5S_2. Less is known about Venus, but its similar size and location in the solar system to Earth indicate that Venus and Earth may have a similar composition (Aitta 2012). Venus' core may still be fully molten, likely because of the lack of a magnetic field and heat release through plate tectonics (Nimmo et al. 2002), lending little constraint on how the core light element composition attributes to the core structure.

With this limited knowledge of Venus' deep interior, we applied the same core-crystallization model to the pressure range of Venus' core assuming a similar Fe-rich composition of Venus' core to that of Earths'. For the model to begin crystallizing a denser inner core, the starting bulk sulfur content of Venus' core is limited to < ~ 5 wt% S (Mori et al., 2017) (Figure 5b). It is possible that Venus' core is more light-element rich than Earth's, and this model represents a minimum depth of Fe-sulfide crystallization. The pressure-eutectic-composition relationship for the Fe-S system from Mori et al. (2017) was used to track the liquid

core composition during crystallization. We then parameterized the pressure-depth relationship for Earth's liquid outer core (Dziewonski and Anderson, 1981) and applied it to the pressure range of Venus' liquid core for comparison of the depths of Fe_5S_2 and Fe_3S crystallization. Results from this calculation constrain the onset of Fe-sulfide crystallization in Venus' core above 170 GPa. Fe + Fe_5S_2 would crystallize from 170 – 120 GPa, associated with approximately 4800 km – 4200 km, and Fe + Fe_3S crystallization occurs above the depth of 120 GPa and extends to the CMB (Figure 5b). Crystallization of Fe_3S would be observed in the outer ~75 km shell of Venus' core (Figure 5b). Bulk core S contents of $\leq$ 1 wt% are required to maintain a sufficiently Fe-rich liquid to 120 GPa, such that only Fe + Fe_3S would deposit in the Venusian core (Figure 5b).

These models suggest that Earth's and Venus' future fully crystallized core will contain a significant portion of Fe_5S_2. Fe_5S_2 will be the only sulfide to crystallize in Earth's core while a distinct layer of Fe_3S is likely to crystallize at the top of Venus' core. ~~such that~~ The details of the Fe_5S_2 crystalline structure in comparison to that of Fe_3S and other crystallizing phases are essential to characterizing the electronic and elastic properties of Earth's and Venus' crystallized cores. Fe_5S_2 exhibits significantly increased metal-metal bonding compared to other iron-alloy phases at core pressures (Figure S2; Tables 3, S2), with Fe in ~5-fold coordination with other Fe sites, based on a linear extrapolation of Fe-Fe bonds with pressure (Fei et al., 2000; Ishimatsu et al., 2021). This marks a ~40% increase in the number of Fe-Fe interactions compared to Fe_3S at similar pressures and interatomic distances. Fe + Fe_5S_2 deposition may therefore contribute to signatures of higher conductivity compared to other solidified alloy phases that exhibit less Fe-Fe coordination at core conditions. Owing to the complexity of Fe_5S_2 atomic arrangement and the stacking variations and positional disorder observed only along the *c* direction, Fe_5S_2 may also

express significant differences in elastic properties along the *c* versus *a* direction. If this is the case, preferred orientation of crystallized Fe_5S_2 in the outer third of Earth's core (Figure 5a), could have strong effects on seismic wave propagation, especially if Fe_5S_2 + hcp-Fe co-crystallize with their respective seismically fast and slow directions aligned (e.g., Antonangeli et al., 2004). While the electrical properties and seismic properties of Fe_5S_2 are not determined in the present study, the discovery of Fe_5S_2 should prompt future experimental and *ab-initio* work exploring these properties for Fe - Fe_5S_2 alloys at core conditions for comparisons to seismic and electronic signatures in the solid portions of planetary cores.

4.3 Fe_5S_2 in Earth and Planetary multicomponent cores

Terrestrial core chemistries are multicomponent, and Si and Ni are also important core-alloying elements in planets such as Earth, drawing attention to the potential stability of the perryite $(Fe, Ni)_8(Si, P)_3$ structure in (Fe, Ni) – (Si, S)-rich cores. Perryite, observed in enstatite chondrites and aubrites, adopts a trigonal stacking variant of the Ni_5As_2-type structure (Wasson and Wai, 1970; Okada et al. 1991), and iron phosphides tend to adopt analog structures to those observed in iron sulfides (i.e., Fei et al. 2000; Dera et al. 2008; Gu et al. 2014; Gu et al. 2016; Zurkowski et al., in press). Hence, Fe_5S_2 could potentially serve as a host for nickel and silicon in its perryite-like structure at Earth's outer core conditions. Silicon has also recently been shown to dissolve into iron-sulfide phases and expand their stability field to higher pressure (Tao and Fei, 2021). The dissolution of silicon into Fe_5S_2 may extend its stability to higher pressures, making it potentially relevant at Earth's ICB conditions. If this is the case, the partitioning of Si and Ni between $(Fe, Ni)_5(S, Si)_2$ and (Fe, Ni, Si)-metal and the density difference between the

463 inner-core-crystallizing phase and remaining light-element-rich liquid will be crucial to
464 investigations of the inner-core-density deficit and inner core seismic morphology.
465

466 # 5. CONCLUSIONS

467 To assess the phase stability of Fe-rich sulfides at Earth's outer core conditions, Fe-rich
468 sulfide compositions were examined to 200 GPa and 3250 K using single-crystal and powder X-
469 ray diffraction techniques in a laser-heated diamond anvil cell. At high temperatures between
470 120 and 200 GPa, Fe_5S_2 is synthesized in the Ni_5As_2-type structure. The atomic arrangement of
471 this hexagonal structure is characterized by positional disorder, complex coordination
472 environments and significant Fe-Fe interactions. Along with Fe_5S_2, grains of *I*-4 Fe_3S, *C*23 Fe_2S,
473 and *C*37 Fe_2S were also identified at lower temperatures across the pressure range probed. The
474 stability of tetragonal Fe_3S in Fe-rich systems is constrained to below 120 GPa, while between
475 120 and 200 GPa at to 3500 K, Fe_5S_2 is stable coexisting with Fe. Fe_5S_2 is expected to be the
476 only sulfide to crystallize during the freezing of Earth's core, while Venus' core may crystallize
477 predominantly Fe + Fe_5S_2 with an outermost shell of Fe + Fe_3S. The crystallographic
478 complexities of Fe_5S_2 and plausible incorporation of Ni and Si necessitate further investigations
479 into the electronic, seismic, and chemical properties of Fe_5S_2 in multi-component core-systems.
480

481 ## Acknowledgments

482 Portions of this work were performed at GeoSoilEnviroCARS (The University of Chicago,
483 Sector 13), Advanced Photon Source (APS), Argonne National Laboratory.
484 GeoSoilEnviroCARS is supported by the National Science Foundation - Earth Sciences (EAR -

1634415). This research used resources of the Advanced Photon Source, a U.S. Department of Energy (DOE) Office of Science User Facility operated for the DOE Office of Science by Argonne National Laboratory under Contract No. DE-AC02-06CH11357. This material is based upon work supported by a National Science Foundation Graduate Research Fellowship to C.C.Z. This work was also supported by the National Science Foundation by grant EAR-1651017 to A.J.C.

6. TABLES

Table 1. Unit cell parameters of Fe_5S_2, Fe_3S, and Fe_2S measured upon quenching from high *P-T* synthesis in this study. Each cell was indexed in the reciprocal space, and the DAC opening, and number of reflections obtained for each lattice are listed. For select experiments, high-temperature synthesis was conducted without collecting X-ray diffraction data, and the synthesis conditions for these experiments are listed as "high T, not measured." Synthesis times varied from ~30-45 minutes.

			Room temperature collection								Synthesis conditions	
Sample name	**Start comp.**	**Med.**	**Phase**	**P** GPa	***a*** Å	***b*** Å	***c*** Å	**V** Å^3	***ω*** º	**Refl.**	***P*** GPa	***T*** K
C140_P2_map25	$Fe_{80}S_{20}$	KCl	Fe_5S_2	105(2)	6.020(4)		11.204(7)	351.6(5)	60	290	119(2)	2840(140)
C140_P2_map31	$Fe_{80}S_{20}$	KCl	Fe_5S_2	105(2)	6.050(2)		73.0(2)	2313(1)	60	134	119(2)	2840(140)
C140_P4_map10	$Fe_{80}S_{20}$	KCl	Fe_5S_2	118(1)	5.983(3)		11.078(6)	343.4(4)	60	489	140(2)	3070(180)
C140_P4_map14	$Fe_{80}S_{20}$	KCl	Fe_5S_2	118(1)	5.979(2)		11.084(4)	343.2(3)	60	379	140(2)	3070(180)
C140_P4_map14	$Fe_{80}S_{20}$	KCl	Fe_5S_2	118(1)	5.973(1)		11.094(2)	342.8(1)	60	276	140(2)	3070(180)
C129_P140_map71	$Fe_{67}S_{33}$	SiO_2	Fe_5S_2	136.4(5)	5.957(4)		71.89(4)	2209(3)	34	84	159(2)	3230(150)
C129_P150_map9	$Fe_{67}S_{33}$	SiO_2	Fe_5S_2	144.2(8)	5.939(3)		25.99(6)	794(2)	34	76	high T, not measured	
C129_P150_map9	$Fe_{67}S_{33}$	SiO_2	Fe_5S_2	144.2(8)	5.923(1)		26.004(6)	789.9(3)	34	146	high T, not measured	
C137_P1_map25	$Fe_{80}S_{20}$	SiO_2	Fe_5S_2	159(1)	5.890(3)		25.837(7)	776.2(5)	40	108	184(3)	3250(260)
C137_P1_map25	$Fe_{80}S_{20}$	SiO_2	Fe_5S_2	159(1)	5.880(1)		25.789(3)	772.0(2)	40	108	184(3)	3250(260)
C137_P1_map25	$Fe_{80}S_{20}$	SiO_2	Fe_5S_2	159(1)	5.876(2)		25.884(8)	774.0(4)	40	116	184(3)	3250(260)
C137_P1_map25	$Fe_{80}S_{20}$	SiO_2	Fe_5S_2	159(1)	5.883(3)		25.85(1)	774.6(7)	40	126	184(3)	3250(260)
C137_P1	$Fe_{80}S_{20}$	SiO_2	Fe_5S_2	159(1)	5.897(3)		25.90(1)	775.1(6)	40	116	184(3)	3250(260)
C137_P1	$Fe_{80}S_{20}$	SiO_2	Fe_5S_2	159(1)	5.878(1)		25.784(3)	771.6(2)	40	149	184(3)	3250(260)
C137_P2_34	$Fe_{80}S_{20}$	SiO_2	Fe_5S_2	179(1)	5.8400(7)		25.583(2)	755.7(1)	40	189	193(4)	3010(160)
C140_P1_map	$Fe_{80}S_{20}$	KCl	Fe_3S	100(1)	8.156(3)		4.025(3)	267.8(3)	60	416	high T, not measured	
C140_P2_map25	$Fe_{80}S_{20}$	KCl	Fe_3S	105(2)	8.094(3)		3.990(2)	261.4(2)	60	296	119(2)	2840(140)
C140_P3_map6	$Fe_{80}S_{20}$	KCl	*C*23 Fe_2S	111(1)	4.869(2)	3.256(2)	6.139(2)	97.3(1)	60	227	131(2)	3050(140)
C140_P4_map10	$Fe_{80}S_{20}$	KCl	*C*37 Fe_2S	118(1)	4.677(2)	3.289(1)	6.186(4)	95.18(9)	60	188	140(2)	3070(180)

Table 2. Atomic coordinates of the Fe_5S_2 refinement model for the data collected at 140(2) GPa and quenched from 3070(180) K.

Wyckoff site	ATOM	x	y	z	Uiso
2a	**Fe1**	0	0	0.963	0.021
	error			0.003	0.005
4b	**Fe2**	1/3	2/3	0.089	0.046
	error			0.003	0.005
6c	**Fe3**	0.259	0	0.126	0.021
	error	0.002		0.001	
6c	**Fe4**	0.613	0	0.222	0.021
	error	0.002		0.001	0.003
6c	**Fe5**	0.284	0	0.330	0.027
	error	0.002		0.001	0.003
12d	**Fe6***	0.651	0.056	0.426	0.021
	error	0.003	0.003	0.002	
2a	**S1**	0	0	0.220	0.026
	error			0.004	
4b	**S2**	1/3	2/3	0.299	0.026
	error			0.002	
6c	**S3**	0.673	0	0.030	0.026
	error	0.005		0.003	

*indicates half occupancy

Table 3. Selected interatomic distances for the Fe sites measured in Fe_5S_2 at 140 GPa. The "#" column indicates that number of the "bonded to" sites around the central atom.

Atom	bonded to	#	distance (Å)
Fe1	–Fe3	3	2.39(2)
	–Fe5	3	2.22(3)
	–Fe6	3	2.313(17)
	–S1	1	2.66(8)
	–S4	3	2.09(3)
Fe2	–Fe3	3	2.275(3)
	–Fe4	3	2.375(16)
	–Fe6	3	2.40(3)
	–S3	1	2.36(4)
	–S4	3	2.108(13)
Fe3	–Fe1	1	2.39(2)
	–Fe2	2	2.275(8)
	–Fe4	3	2.350(15)
	–Fe5	1	2.30(3)
	–Fe6	1	2.307(17)
	–S1	1	1.90(4)
	–S4	3	2.68(3)
Fe4	–Fe2	2	2.375(16)
	–Fe3	3	2.320(11)
	–Fe5	3	2.416(14)
	–Fe6	1	2.303(17)
	–S1	1	2.326(11)
	–S3	2	2.044(16)
	–S4	1	2.10(3)
Fe5	–Fe1	1	2.22(3)
	–Fe3	1	2.30(3)
	–Fe4	3	2.416(14)
	–Fe6	3	2.135(15)
	–S1	1	2.09(5)
	–S3	2	2.184(10)
	–S4	1	2.27(3)

Fe6	–Fe1	1	2.313(17)
	–Fe2	2	2.40(3)
	–Fe3	1	2.307(17)
	–Fe4	1	2.303(17)
	–Fe5	3	2.135(15)
	–S3	2	2.15(3)
	–S4	3	2.17(3)

Figures

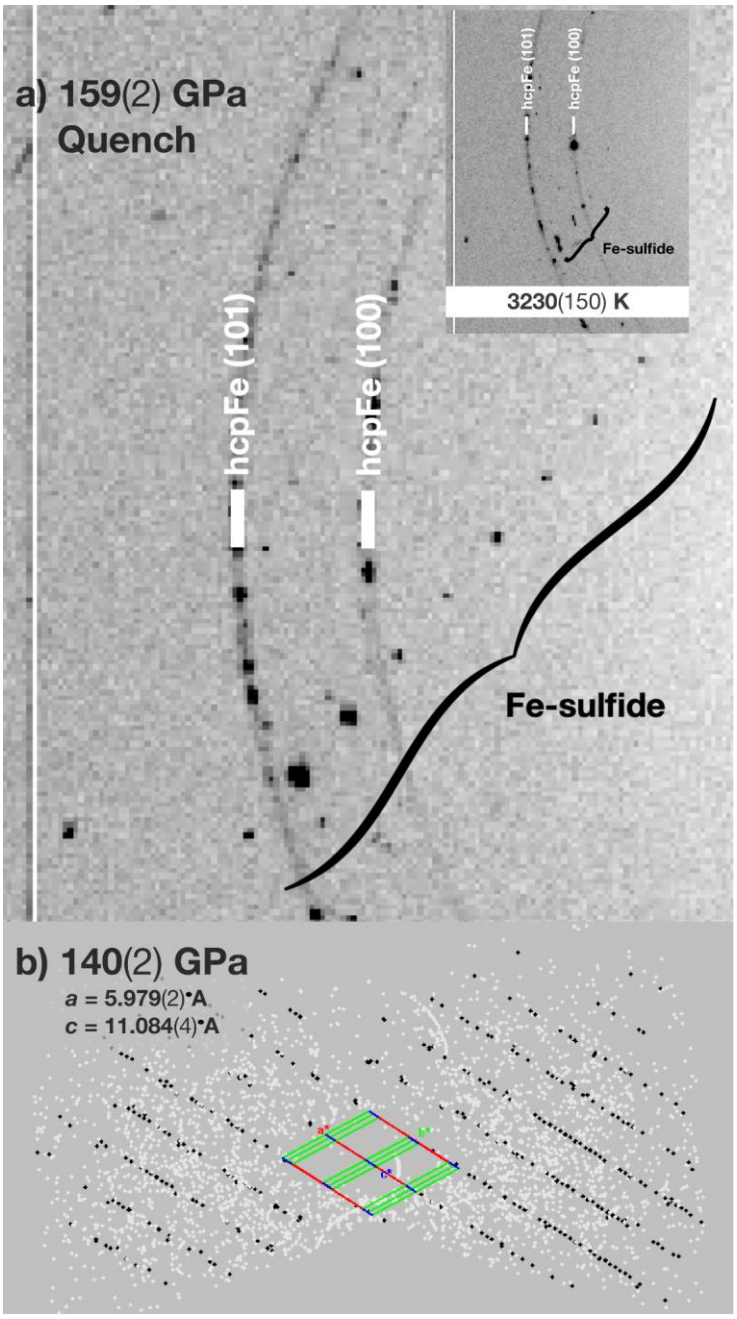

Figure 1. a) Diffraction from a crystallite of the high-temperature Fe_5S_2 coexisting with recrystallized hcp-Fe after synthesis at 159(2) GPa and 3230(130) K (inset). The spotty rings corresponding to the hcp-Fe (100) and (101) planes demonstrate that iron equilibrated at 159(2) GPa and 3230(130) K. b) View of the reciprocal space for reflections detected in an experiment on the $Fe_{80}S_{20}$ composition quenched from 140(2) GPa and 3070(140) K. The reciprocal lattice, colored in black, is associated with a Fe_5S_2 grain whose lattice parameters are provided in the top left.

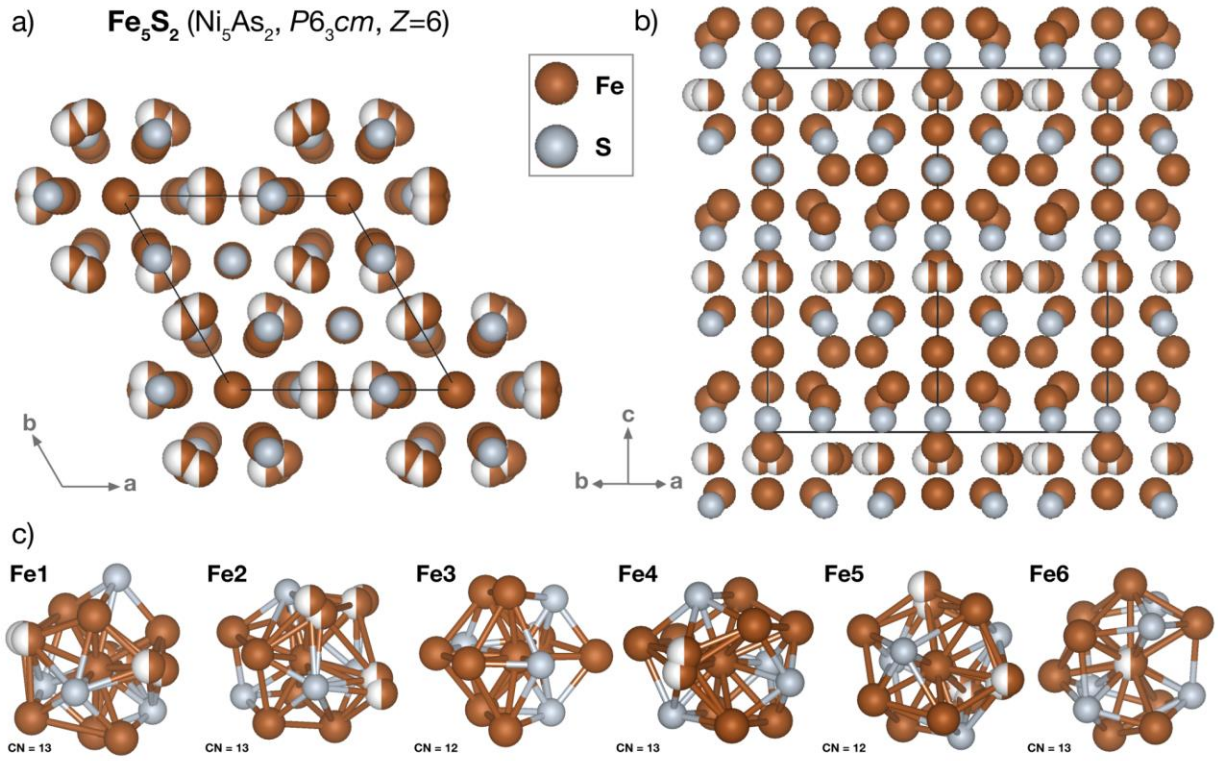

Figure 2. Crystal structure of Fe_5S_2 viewed along the a) *c* axis and the b) (100) plane. c) The Fe-coordination polyhedra observed in this atomic arrangement are provided. Fe1, Fe2, Fe4, and Fe6 are coordinated by 13 sites and Fe3 and Fe5 are coordinated by 12 sites. Each coordination polyhedron consists of Fe and S sites. Crystal-structure graphics were made using Vesta (Momma and Izumi 2011).

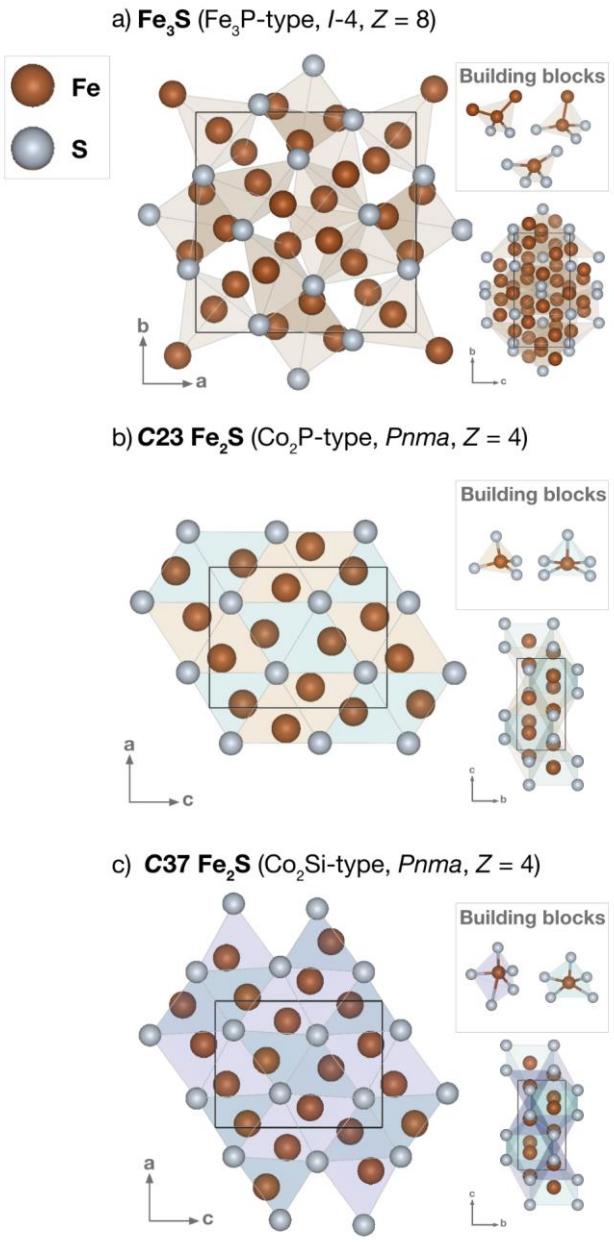

Figure 3. Crystal structures of Fe_3S and Fe_2S observed in this study. a) Fe_3S adopts the Fe_3P-type structure (*I*-4, *Z* = 8) that is composed of three tetrahedrally coordinated Fe-sites, each with increasing Fe–Fe bonding. b) The *C*23 Fe_2S structure (Co_2P-type, *Pnma*, *Z* = 4) is made up of columns of FeS_4 tetrahedra and columns of FeS_5 square pyramids linked along edges in the *b* direction. c) The *C*37 Fe_2S structure (Co_2Si-type, *Pnma*, *Z* = 4) has the same site symmetries as the *C*23 structure, but is marked by a shortened *a* axis and elongated *b* and *c* axes accompanied by the formation of a 5-fold dipyramid. Crystal-structure graphics were made using Vesta (Momma and Izumi 2011).

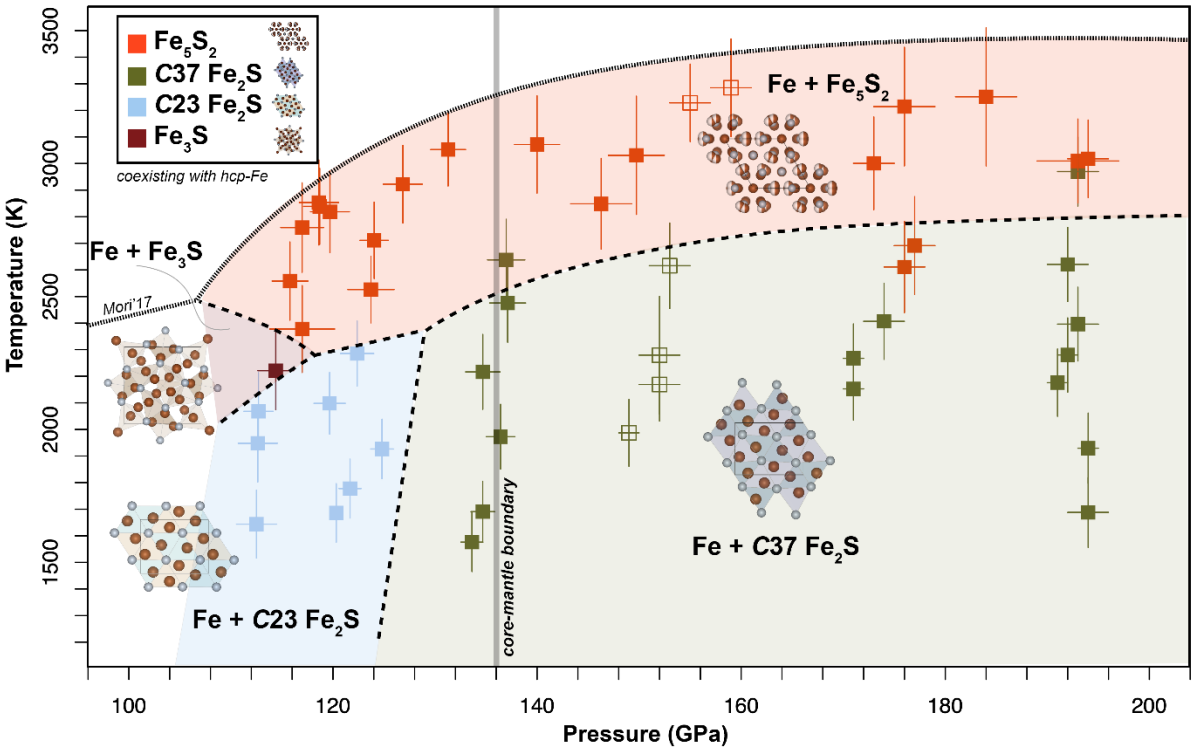

Figure 4. Iron metal-saturated sulfide phase diagram based on the coexisting phases observed in this study. moderate temperatures, Fe_3S is observed below 120 GPa, *C*23 Fe_2S is observed below 130 GPa, and *C*37 Fe_2S is observed above 130 GPa. At high temperatures to 200 GPa, Fe_5S_2 is stable, and a kink in the Fe-S solidus curve (Mori et al., 2017) is presented to account for the change from Fe_3S to Fe_5S_2 melting in Fe-rich systems above ~120 GPa. The closed squares represent experiments conducted on the $Fe_{80}S_{20}$ starting material, and the open squares represent experiments conducted on the $Fe_{67}S_{33}$ starting material. Both show compatible results and iron recrystallization at high temperatures, indicating that Fe-rich regions of the $Fe_{67}S_{33}$ foils were probed.

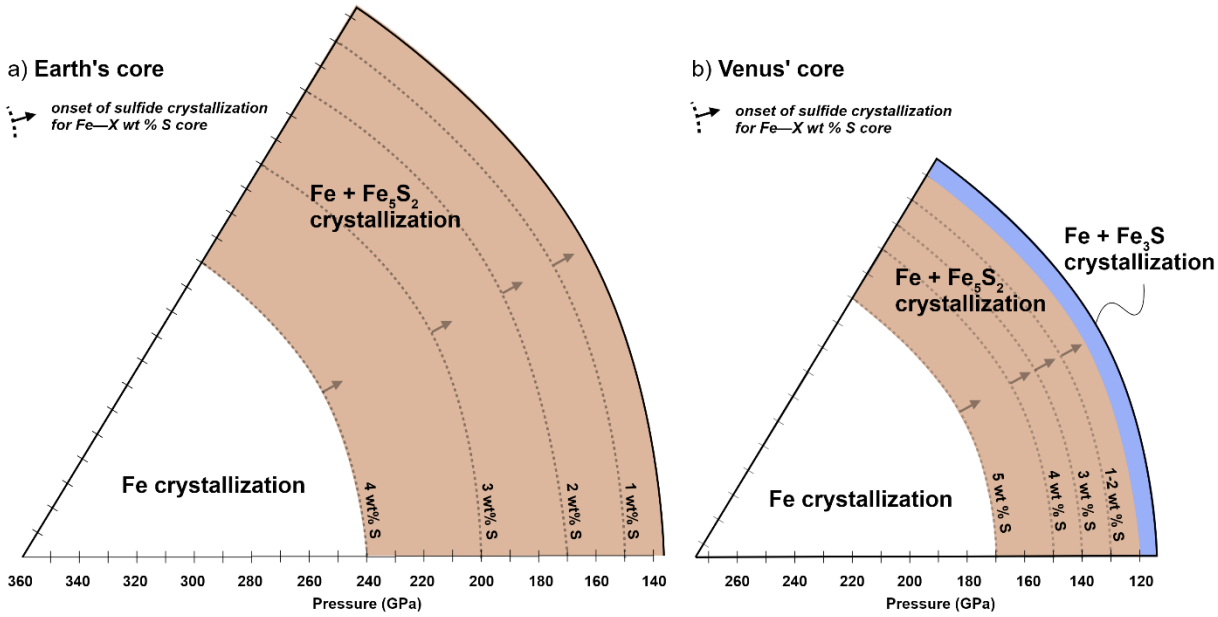

Figure 5. Models of a) Earth's and b) Venus' core Fe-S crystallization using sulfur contents that satisfy Fe inner core crystallization following Mori et al., (2017), cosmochemical approximations (McDonough and Sun 1995), and metal-silicate partitioning studies (Suer et al., 2017). Each dashed curve represents the pressure at which the sulfur content of the outer core liquid becomes sulfur rich of the Fe-saturated Fe-S eutectic (Mori et al., 2017) and begins crystallizing Fe + Fe_5S_2 (red) or Fe + Fe_3S (blue) for a bulk Fe—*X* wt % S core with *X* values labeled at the base of each curve.

8. SUPPLEMENTAL

This supplementary information file includes the experimental, crystal-structure analysis, and structural information for the Fe_5S_2, Fe_3S, and Fe_2S phases presented in this work. Supplemental tables provide the synthesis conditions, unit cell geometries, refinement statistics, and interatomic distances measured for each phase. The supplemental figures depict diffraction from the novel Fe_5S_2 phase, the range of Fe-S distances measured among the iron-sulfides presented, a visual comparison of the related Fe_2S polymorphs, and changes in phase relationships among the iron-sulfides via integrated diffraction patterns.

Table S1. Select experimental details for crystal structure synthesis and analysis of Fe_5S_2, Fe_3S, and the Fe_2S polymorphs.

Phase	**Fe_5S_2**	**Fe_3S**	***C*23 Fe_2S**	***C*37 Fe_2S**
Sample Name	**C140_P4_map10**	**C140_P2_map25**	**C140_P3_map 6**	**C140_P4_map10**
Synthesis				
Pressure (GPa)	140(2)	119(2)	131(2)	140(2)
Synthesis Temperature (K)	3070(180)	2840(140)	2050(140)	3070(180)
Symmetry	Hexagonal, *P*6(3)*cm*, Z=6	Tetragonal, *I*-4, Z=8	Orthorhombic, *Pnma*, *Z* = 4	Orthorhombic, *Pnma*, *Z* = 4
a (Å)	5.979(2)	8.094(3)	4.869(3)	4.677(2)
b (Å)			3.256(4)	3.289(1)
c (Å)	11.087(6)	3.990(2)	6.139(2)	6.186(4)
V (Å^3)	343.2(3)	226.4(2)	97.3(1)	95.18(9)
Reduction				
No. of measured, independent and observed [I > 2σ(I)] reflections	396, 309, 157	332, 314, 219	227, 208, 112	188, 158, 105
R_{int}, R_{sigma}	0.092, 0.062	0.053, 0.072	0.012, 0.016	0.009, 0.014
Refinement				
$R[F^2 > 2\sigma(F^2)]$, $wR(F^2)$, *S*	0.098, 0.255, 1.12	0.067, 0.164, 1.05	0.053, 0.149, 1.21	0.047, 0.139, 1.22
No. of reflections	156	219	112	105
No. of parameters	21	17	10	10
$\Delta\rho_{max}$, $\Delta\rho_{min}$ (e Å^{-3})	2.14, -2.18	1.92, -1.68	1.86, -2.02	1.91, -2.21

Table S2. Fe_3S interatomic distances measured at 119(2) GPa.

Central	Bond	Length (Å)	Error (Å)
Fe1	S1	2.028	0.008
Fe1	S1	2.085	0.009
Fe1	Fe1	2.16	0.008
Fe1	Fe3	2.273	0.006
Fe1	Fe3	2.391	0.006
Fe1	Fe3	2.4	0.006
Fe1	Fe2	2.406	0.006
Fe1	Fe1	2.414	0.007
Fe1	Fe1	2.414	0.007
Fe1	Fe3	2.509	0.006
Fe1	Fe2	2.537	0.006
Fe1	Fe3	2.565	0.006
Fe2	S1	2.06	0.009
Fe2	S1	2.071	0.008
Fe2	S1	2.083	0.008
Fe2	S1	2.119	0.009
Fe2	Fe3	2.294	0.006
Fe2	Fe3	2.306	0.006
Fe2	Fe2	2.316	0.009
Fe2	Fe3	2.346	0.006
Fe2	Fe1	2.406	0.006
Fe2	Fe2	2.482	0.007
Fe2	Fe2	2.482	0.007
Fe2	Fe1	2.536	0.006
Fe3	S1	2.026	0.008
Fe3	S1	2.068	0.008
Fe3	S1	2.219	0.009
Fe3	Fe1	2.273	0.006
Fe3	Fe2	2.294	0.006
Fe3	Fe3	2.343	0.004
Fe3	Fe3	2.343	0.004
Fe3	Fe2	2.346	0.006
Fe3	Fe1	2.4	0.006
Fe3	Fe1	2.509	0.006

Table S3. *C*23 Fe_2S interatomic distances measured at 131(2) GPa.

Central	Bond	Length (Å)	Error (Å)
Fe1	S1	2.101	0.003
Fe1	S1	2.136	0.003
Fe1	S1	2.136	0.003
Fe1	S1	2.326	0.003
Fe1	S1	2.326	0.003
Fe1	Fe2	2.356	0.002
Fe1	Fe2	2.356	0.002
Fe1	Fe2	2.398	0.002
Fe1	Fe2	2.398	0.002
Fe1	Fe2	2.411	0.003
Fe1	Fe2	2.415	0.002
Fe1	Fe2	2.5594	0.002
Fe2	S1	1.997	0.003
Fe2	S1	2.037	0.004
Fe2	S1	2.045	0.002
Fe2	S1	2.045	0.002
Fe2	Fe2	2.351	0.003
Fe2	Fe2	2.351	0.003
Fe2	Fe1	2.356	0.002
Fe2	Fe1	2.356	0.002
Fe2	Fe1	2.398	0.002
Fe2	Fe1	2.398	0.002
Fe2	Fe1	2.411	0.003
Fe2	Fe1	2.415	0.002

Table S4. *C*37 Fe_2S interatomic distances measured at 140(2) GPa.

Central	Bond	Length (Å)	Error (Å)
Fe1	S1	2.097	0.003
Fe1	S1	2.1094	0.002
Fe1	S1	2.1094	0.002
Fe1	Fe2	2.3286	0.002
Fe1	Fe2	2.3286	0.002
Fe1	S1	2.331	0.002
Fe1	S1	2.331	0.002
Fe1	Fe2	2.377	0.002
Fe1	Fe2	2.3793	0.002
Fe1	Fe2	2.3793	0.002
Fe1	Fe2	2.398	0.003
Fe1	Fe1	2.4436	0.001
Fe2	S1	2.014	0.003
Fe2	S1	2.019	0.003
Fe2	S1	2.0506	0.002
Fe2	S1	2.0506	0.002
Fe2	S1	2.690	0.003
Fe2	Fe1	2.3286	0.002
Fe2	Fe1	2.3286	0.002
Fe2	Fe2	2.3674	0.002
Fe2	Fe2	2.3674	0.002
Fe2	Fe1	2.377	0.002
Fe2	Fe1	2.3792	0.002
Fe2	Fe1	2.3792	0.002
Fe2	Fe1	2.398	0.003

Figure S1. Unwarped diffraction mappings of the (1*kl*), (0*kl*), and (-1*kl*) directions for an Fe_5S_2 crystallite exemplifying the diffuse scattering signal collected at 119(2) and 2840(180) K. The (1*kl*) and (-1*kl*) mappings also show the presence of a polytype with more closely spaced reflections oriented ~51° from the mapped crystallite.

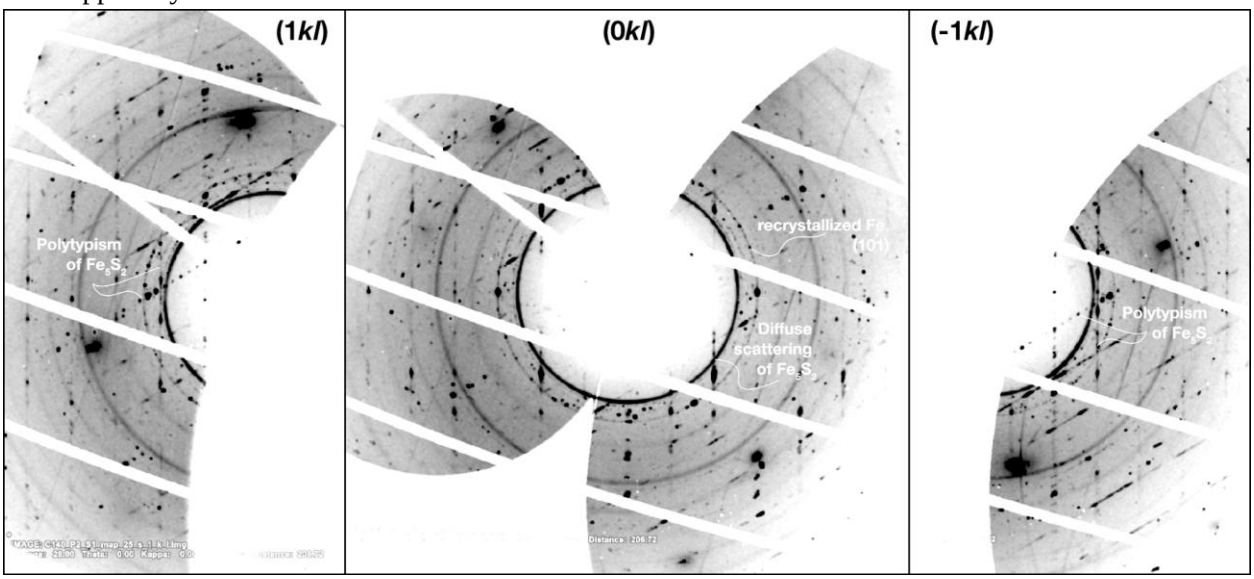

Figure S2. Range of Fe-S (blue) and Fe-Fe (brown) interatomic distances observed in Fe_3S (triangles), *C*23 Fe_2S (circles), *C*37 Fe_2S (crosses), and Fe_5S_2 (squares) based on the pressure at which each structure was refined.

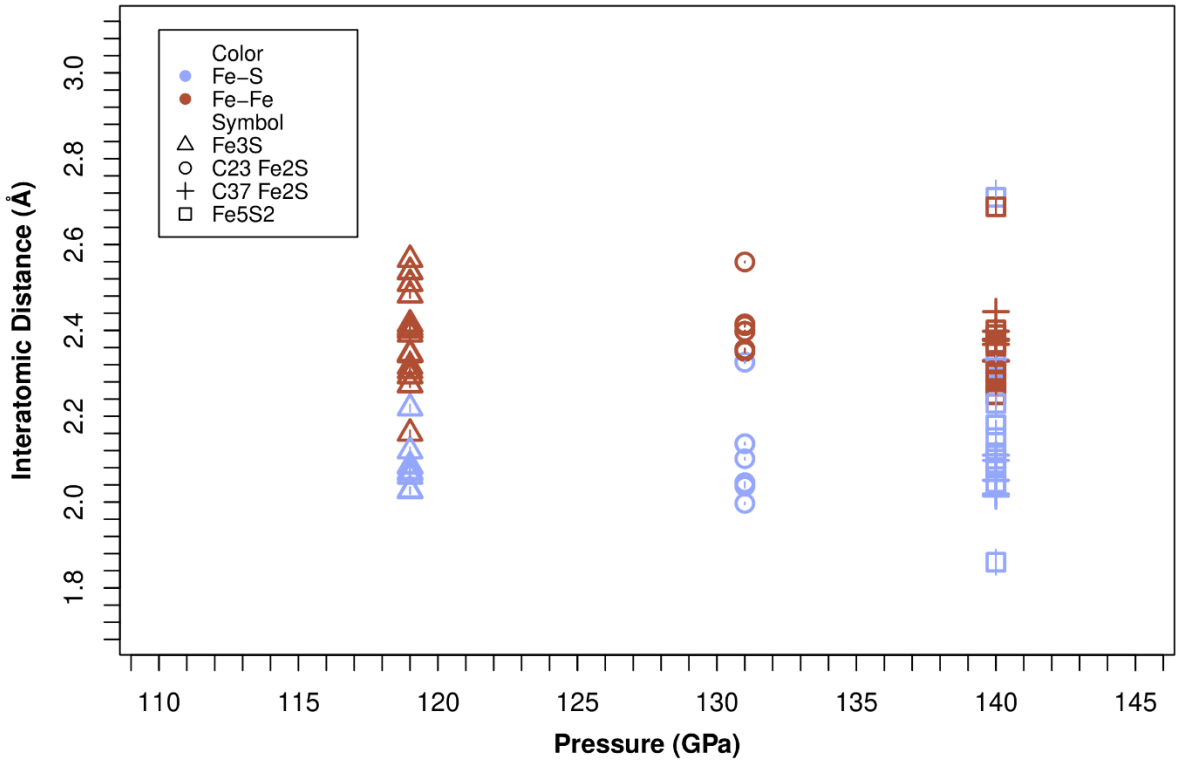

Figure S2. Comparison of the *C*23 and *C*37 Fe_2S structure models refined at 130 and 140 GPa, respectively. In the *C*23 Fe_2S structure, the next nearest sulfur site to the Fe1 tetrahedral site is at a 2.963(1) Å distance at 130 GPa (dotted line). A 10% contraction of this interatomic distance and a coordination change is observed in the formation of *C*37 Fe_2S at 140 GPa (right). Crystal-structure graphics were made using Vesta (Momma and Izumi 2011).

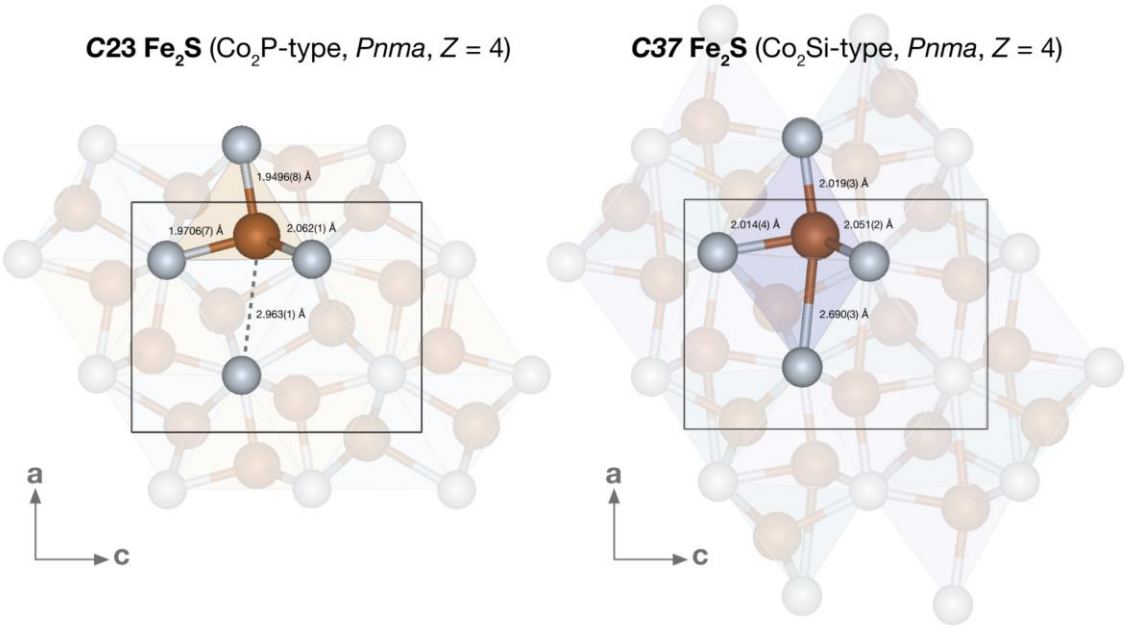

Figure S4. X-ray diffraction patterns collected upon heating in an $Fe_{80}S_{20}$ starting composition at a) 119(2) GPa and b)184(3) GPa. The miller indices for *C*23 Fe_2S (blue), Fe_3S (burgundy), and *C*37 Fe_2S (green) are provided, and the red "H" symbols represent the observations of the formation of Fe_5S_2. The growth of large crystallites, along with the disorder and polytypism of this phase make for challenging powder diffraction indexing, but the lattice parameters of Fe_5S_2 indexed in the reciprocal space after quenching from these high *P*-*T* conditions are provided.

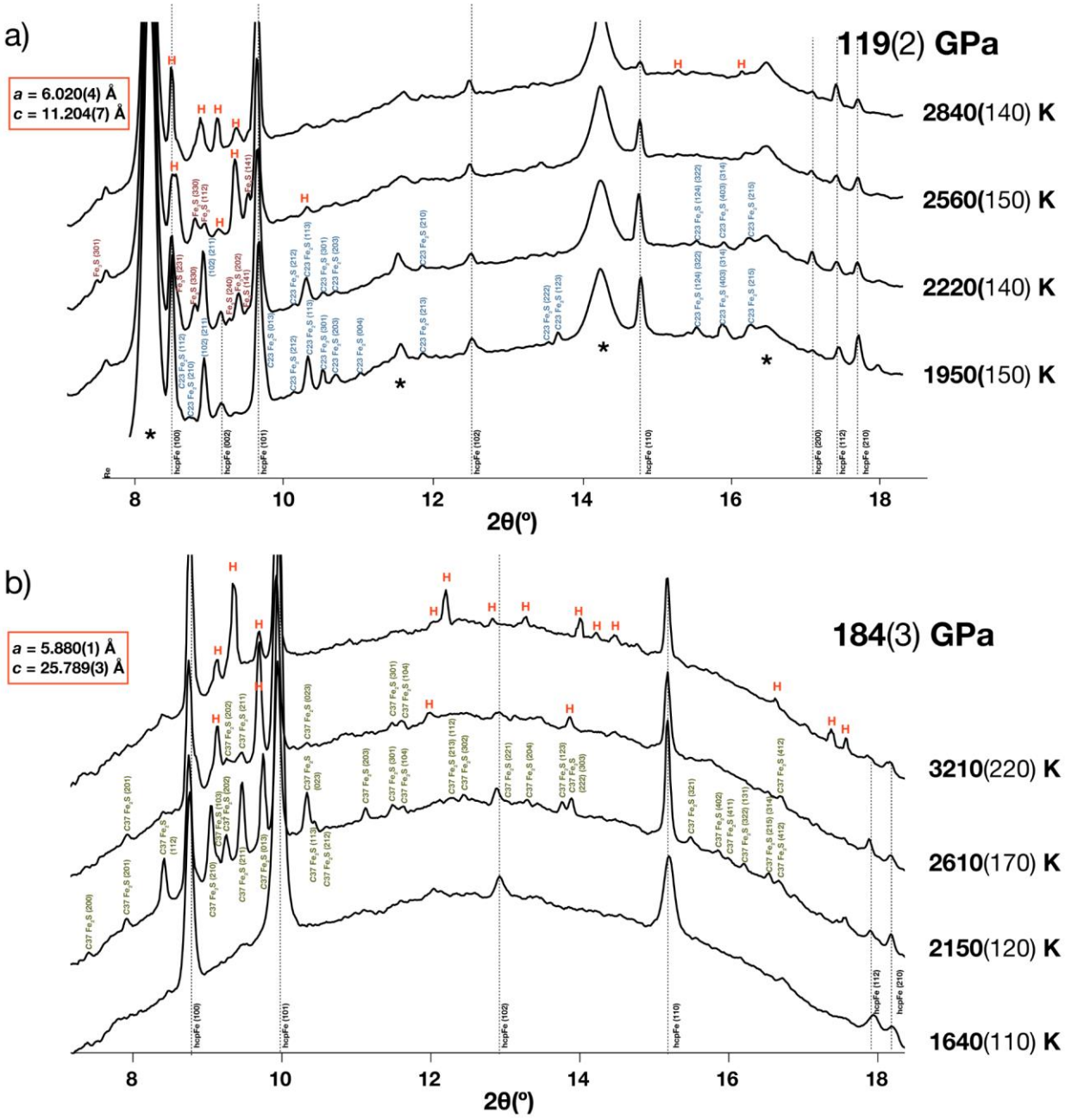

References

Aitta, A., (2012) Venus' internal structure, temperature and core composition. Icarus, 218, 967–974.

Antonangeli, D., Occelli, F., Requardt, H., Badro, J., Fiquet, G. and Krisch, M., (2004), Elastic anisotropy in textured hcp-iron to112 GPa from sound wave propagation measurements, Earth Planet.Sci. Lett., 225, 243–251.

Anzellini, S., Dewaele, A., Mezouar, M., Loubeyre, P. and Morard, G., 2013. Melting of iron at Earth's inner core boundary based on fast X-ray diffraction. Science, 340, 464–466. https://doi.org/10.1126/science.1233514

Birch, F., 1952. Elasticity and constitution of the Earth's interior. J. Geophys. Res., 57, 227–286. https://doi.org/10.1029/JZ057i002p00227

Blanchard, P.E., Grosvenor, A.P., Cavell, R.G. and Mar, A., 2008. X-ray Photoelectron and Absorption Spectroscopy of Metal-Rich Phosphides M_2P and M_3P (M= Cr − Ni). Chem. Mater., 20, 7081–7088. https://doi.org/10.1021/cm802123a

Campbell, A.J., Seagle, C.T., Heinz, D. L., Shen, G., and Prakapenka, V.B., 2007. Partial melting in the iron-sulfur system at high pressure: A synchrotron X-ray diffraction study. Phys. Earth Planet. Inter., 162, 119–128. https://doi.org/10.1016/j.pepi.2007.04.001

Campbell, A.J., Danielson, L., Righter, K., Seagle, C.T., Wang, Y. and Prakapenka, V.B., 2009. High pressure effects on the iron–iron oxide and nickel–nickel oxide oxygen fugacity buffers. Earth Planet. Sci. Lett., 286, 556–564. https://doi.org/10.1016/j.epsl.2009.07.022

Chen, J.H. and Whitmire, K.H., 2018. A structural survey of the binary transition metal phosphides and arsenides of the d-block elements. Coord. Chem. Rev., 355, 271–327. https://doi.org/10.1016/j.ccr.2017.08.029

Dewaele, A., Loubeyre, P., Occelli, F., Mezouar, M., Dorogokupets, P.I. and Torrent, M., 2006. Quasihydrostatic equation of state of iron above 2 Mbar. Phys. Rev., 97, 215504. https://doi.org/10.1103/PhysRevLett.97.215504

Dziewonski, A.M. and Anderson, D.L., 1981. Preliminary reference Earth model. Phys. Earth Planet. Inter., 25, 297–356. https://doi.org/10.1016/0031-9201(81)90046-7

El-Boragy, M., Bhan, S. and Schubert, K., 1970. Kristallstruktur von Pd_5Sb_2 und Ni_5As_2 und einigen varianten. J. less-common met, 22, 445–458. https://doi.org/10.1016/0022-5088(70)90132-3

Evans, H.T., 1970. Lunar troilite: crystallography. Science, 167, 621–623. https://doi.org/10.1126/science.167.3918.621

Fearn, D.R. and Loper, D.E., 1981. Compositional convection and stratification of Earth's core. Nature, 289, 393–394. https://doi.org/10.1038/289393a0

Fei, Y., Prewitt, C.T., Mao, H.K. and Bertka, C.M, 1995. Structure and density of FeS at high pressure and high temperature and the internal structure of Mars. Science, 268, 1892–1894. https://doi.org/10.1126/science.268.5219.1892

Fei, Y., Bertka, C.M. and Finger, L.W., 1997. High-pressure iron-sulfur compound, Fe_3S_2, and melting relations in the Fe–FeS system. Science, 275, 1621–1623.

https://doi.org/10.1126/science.275.5306.1621
Fei, Y., Li, J., Bertka, C.M. and Prewitt, C.T., 2000. Structure type and bulk modulus of Fe_3S, a new iron-sulfur compound. Am. Mineral., 85, 1830–1833. https://doi.org/10.2138/am-2000-11-1229
Fei, Y., Ricolleau, A., Frank, M., Mibe, K., Shen, G. and Prakapenka, V., 2007. Toward an internally consistent pressure scale. Proc. Natl. Acad. Sci. U.S.A., 104, 9182–9186. https://doi.org/10.1073/pnas.0609013104
Frank, K. and Schubert, K., 1971. Kristallstruktur von $Ni_{31}Si_{12}$. Acta crystallogr., B Struct. crystallogr. cryst. chem., 27, 916–920. https://doi.org/10.1107/S0567740871003261
Heinz, D.L., and Jeanloz, R., 1987. Measurement of the melting curve of $Mg_{0.9}Fe_{0.1}SiO_3$ at lower mantle conditions and its geophysical implications. J. Geophys. Res., 92, 437–444. https://doi.org/10.1029/JB092iB11p11437
Irving, J.C., Cottaar, S. and Lekić, V., 2018. Seismically determined elastic parameters for Earth's outer core. Sci. Adv., 4, 2538. https://doi.org/10.1126/sciadv.aar2538
Ishimatsu, N., Iwasaki, S., Kousa, M., Kato, S., Nakajima, N., Kitamura, N., Kawamura, N., Mizumaki, M., Kakizawa, S., Nomura, R. and Irifune, T., 2021. Elongation of Fe-Fe atomic pairs in the Invar alloy $Fe_{65}Ni_{35}$. Phys. Rev. B., 103, L220102. https://link.aps.org/doi/10.1103/PhysRevB.103.L220102
Jephcoat, A. and Olson, P., 1987. Is the inner core of the Earth pure iron? Nature, 325, 332–335. https://doi.org/10.1038/325332a0
Jones, J.H. and Drake, M.J., 1983. Experimental investigations of trace element fractionation in iron meteorites, II: The influence of sulfur. Geochim. Cosmochim. Acta., 47, 1199–1209. https://doi.org/10.1016/0016-7037(83)90062-5
Kamada, S., Terasaki, H., Ohtani, E., Sakai, T., Kikegawa, T., Ohishi, Y., Hirao, N., Sata, N. and Kondo, T., 2010. Phase relationships of the Fe–FeS system in conditions up to the Earth's outer core. Earth Planet. Sci. Lett., 294, 94–100. https://doi.org/10.1016/j.epsl.2010.03.011
Kamada, S., Ohtani, E., Terasaki, H., Sakai, T., Miyahara, M., Ohishi, Y. and Hirao, N., 2012. Melting relationships in the Fe–Fe_3S system up to the outer core conditions. Earth Planet. Sci. Lett., 359, 26–33. https://doi.org/10.1016/j.epsl.2012.09.038
Kamada, S., Ohtani, E., Terasaki, H., Sakai, T., Takahashi, S., Hirao, N. and Ohishi, Y., 2014. Equation of state of Fe_3S at room temperature up to 2 megabars. Phys. Earth Planet. Inter., 228, 106-113. https://doi.org/10.1016/j.pepi.2013.11.001
Kantor, I., Prakapenka, V., Kantor, A., Dera, P., Kurnosov, A., Sinogeikin, S., Dubrovinskaia, N. and Dubrovinsky, L., 2012. BX90: A new diamond anvil cell design for X-ray diffraction and optical measurements. Rev. Sci. Instrum., 83, 125102. https://doi.org/10.1063/1.4768541
King, H. and Prewitt, C.T., 1982. High-pressure and high-temperature polymorphism of iron sulfide (FeS). Acta crystallogr., B Struct. crystallogr. cryst. chem., 8, 1877–1887. https://doi.org/10.1107/S0567740882007523
Kjekshus, A., Skaug, K.E., Hebrew, C., Van Buren, C.T., Klæboe, P. and Swahn, C.G., 1973.

On the crystal structure of Ni_5As_2. Acta Chem. Scand., 27, 582–588.
Kruijer, T.S., Touboul, M., Fischer-Gödde, M., Bermingham, K.R., Walker, R.J. and Kleine, T., 2014. Protracted core formation and rapid accretion of protoplanets. Science, 344, 1150–1154. https://doi.org/10.1126/science.1251766
Kuwayama, Y., Morard, G., Nakajima, Y., Hirose, K., Baron, A.Q., Kawaguchi, S.I., Tsuchiya, T., Ishikawa, D., Hirao, N. and Ohishi, Y., 2020. Equation of state of liquid iron under extreme conditions. Phys. Rev., 124, .165701. https://doi.org/10.1103/PhysRevLett.124.165701
Litasov, K.D., Shatskiy, A.F., Minin, D.A., Kuper, K.E. and Ohfuji, H., 2019. The Ni–Ni_2P phase diagram at 6 GPa with implication to meteorites and super-reduced terrestrial rocks. High Press. Res., 39, 561–578. https://doi.org/10.1080/08957959.2019.1672677
Maaref, S., Madar, R., Chaudouet, P., Fruchart, R., Senateur, J.P., Averbuch-Pouchot, M.T., Bacmann, M., Durif, A. and Wolfers, P., 1983. Etude de la structure et des conditions de stabilite d'un nouvel arseniure de fer: $Fe_{12}As_5$. Mater. Res. Bull., 18, 473-480. https://doi.org/10.1016/0025-5408(83)90139-3
Malvin, D.J., Wang, D. and Wasson, J.T., 1984. Chemical classification of iron meteorites—X. Multielement studies of 43 irons, resolution of group IIIE from IIIAB, and evaluation of Cu as a taxonomic parameter. Geochim. Cosmochim. Acta., 48, 785–804. https://doi.org/10.1016/0016-7037(84)90101-7
Masters, G. and Gubbins, D., 2003. On the resolution of density within the Earth. Phys. Earth Planet. Inter., 140, 159–167. https://doi.org/10.1016/j.pepi.2003.07.008
McDonough, W.F. and Sun, S.S., 1995. The composition of the Earth. Chem. Geol., 120, 223–253. https://doi.org/10.1016/0009-2541(94)00140-4
McDonough, W.F., 2003. Compositional model for the Earth's core. In The Mantle and Core (Ed. R. W. Carlson), Vol. 2 Treatise on Geochemistry (Exec. Eds. H. D. Holland and K. K. Turekian), 547–568.
Momma, K. and Izumi, F., 2011. VESTA 3 for three-dimensional visualization of crystal, volumetric and morphology data. J. Appl. Crystallogr., 44, 1272–1276. https://doi.org/10.1107/S0021889811038970
Morard, G., Andrault, D., Guignot, N., Sanloup, C., Mezouar, M., Petitgirard, S. and Fiquet, G., 2008. In situ determination of Fe–Fe_3S phase diagram and liquid structural properties up to 65 GPa. Earth Planet. Sci. Lett., 620–626. https://doi.org/10.1016/j.epsl.2008.05.028
Mori, Y., Ozawa, H., Hirose, K., Sinmyo, R., Tateno, S., Morard, G. and Ohishi, Y., 2017. Melting experiments on Fe–Fe_3S system to 254 GPa. Earth Planet. Sci. Lett., 464 135–141. https://doi.org/10.1016/j.epsl.2017.02.021
Murthy, V.R. and Hall, H.T., 1970. The chemical composition of the earth's core: Possibility of sulfur in the core. Phys. Earth Planet. Inter., 2, 276–282. https://doi.org/10.1016/0031-9201(70)90014-2
Nimmo, F., 2015. Thermal and compositional evolution of the core. In Core Dynamics (Ed. Peter Olsen). Vol. 8 Treatise on Geophysics, (Exec. Eds. G. Schubert), 217–241.

834 Okada, A., Kobayashi, K., Ito, T. and Sakurai, T., 1991. Structure of synthetic perryite,
835 $(Ni, Fe)_8(Si, P)_3$. Acta Crystallogr. C Struct. Chem., 47, 1358–1361.
836 https://doi.org/10.1107/S0108270191000483
837 Oryshchyn, S., Babizhetskyy, V., Zhak, O., Stoyko, S., Guérin, R., and Simon, A., 2011. Crystal
838 structure of HT-Ni_5P_2 and reinvestigation of isotypic Ni_5As_2. Intermetallics, 19,
839 1041–1046. https://doi.org/10.1016/j.intermet.2011.03.013
840 Ozawa, H., Hirose, K., Suzuki, T., Ohishi, Y. and Hirao, N., 2013. Decomposition of Fe_3S
841 above 250 GPa. Geophys. Res. Lett., 40, 4845–4849. https://doi.org/10.1002/grl.50946
842 Prakapenka, V.B., Kubo, A., Kuznetsov, A.Laskin, A., Shkurikhin, O., Dera, P., Rivers, M. L.
843 and Sutton, S.R., 2008. Advanced flat top laser heating system for high pressure research
844 at GSECARS: application to the melting behavior of germanium. High Press. Res., 28,
845 225–235. https://doi.org/10.1080/08957950802050718
846 Prescher, C., and Prakapenka, V.B., 2015. DIOPTAS: a program for reduction of two
847 dimensional X-ray diffraction and data exploration. High Press. Res., 35(3), 223– 230.
848 https://doi.org/10.1080/08957959.2015.1059835
849 Ricard, Y., Šrámek, O. and Dubuffet, F., 2009. A multi-phase model of runaway core–mantle
850 segregation in planetary embryos. Earth Planet. Sci. Lett., 284, 144–150.
851 https://doi.org/10.1016/j.epsl.2009.04.021
852 Rigaku Oxford Diffraction, 2018. CrysAlisPRO software system, ver. 1.171.39.44a Rigaku
853 Corporation, Oxford, U.K.
854 Ringwood, A.E., 1966. The chemical composition and origin of the Earth. Advances in earth
855 science, 65, 287.
856 Rubie, D.C., Frost, D.J., Mann, U., Asahara, Y., Nimmo, F., Tsuno, K., Kegler, P., Holzheid, A.
857 and Palme, H., 2011. Heterogeneous accretion, composition and core–mantle
858 differentiation of the Earth. Earth Planet. Sci. Lett., 301, 31–42.
859 https://doi.org/10.1016/j.epsl.2010.11.030
860 Rundqvist, S., 1960. The structures of Co_2P, Ru_2P and related phases. Acta Chem.
861 Scand., 14, 1961–1979.
862 Rundqvist, S. and Jellinek, F., 1959. The structures of Ni_6Si_2B, Fe_2P and some related phases.
863 Acta Chem. Scand., 13, 425–432.
864 Saini, G.S., Calvert, L.D., and Taylor, J.B., 1964. Compounds of the type M_5X_2: Pd_5As_2, Ni_5Si_2,
865 and Ni_5P_2. Can. J. Chem., 42, 1511–1517. https://doi.org/10.1139/v64-233
866 Scott, E.R. and Wasson, J.T., 1975. Classification and properties of iron meteorites. Rev.
867 Geophys., 13, 527–546. https://doi.org/10.1029/RG013i004p00527
868 Seagle, C.T., Campbell, A.J., Heinz, D.L., Shen, G. and Prakapenka, V.B., 2006. Thermal
869 equation of state of Fe_3S and implications for sulfur in Earth's core. J. Geophys. Res. Solid
870 Earth, 111. https://doi.org/10.1029/2005JB004091
871 Shannon, M.C. and Agee, C.B., 1996. High pressure constraints on percolative core formation.
872 Geophys. Res. Lett., 23, 2717–2720. https://doi.org/10.1029/96GL02817
873 Sheldrick, G.M., 2015. Crystal structure refinement with SHELXL. Acta Crystallogr. C Struct.

Chem., 71, 3–8. https://doi.org/10.1107/S2053229614024218
Suer, T.A., Siebert, J., Remusat, L., Menguy, N. and Fiquet, G. (2017) A sulfur-poor terrestrial core inferred from metal–silicate partitioning experiments. Earth and Planetary Science Letters, 469, 84–97.
Stevenson, D.J., 1981. Models of the Earth's core. Science, 214, 611–619. https://doi.org/10.1126/science.214.4521.611
Stevenson, D.J., 1988. Fluid dynamics of core formation. In Topical Conference Origin of the Earth (Vol. 681, p. 87).
Tateno, S., Ozawa, H., Hirose, K., Suzuki, T., I-Kawaguchi, S., and Hirao, N., 2019. Fe_2S: the most Fe-rich iron sulfide at the Earth's inner core pressures. Geophys. Res. Lett., 46, 11,944–11,949. https://doi.org/10.1029/2019GL085248
Wasson, J.T. and Wai, C.M., 1970. Composition of the metal, schreibersite and perryite of enstatite achondrites and the origin of enstatite chondrites and achondrites. Geochim. Cosmochim. Acta, *34*, 169-184. https://doi.org/10.1016/0016-7037(70)90004-9
Yoshino, T., Walter, M.J. and Katsura, T., 2003. Core formation in planetesimals triggered by permeable flow. Nature, 422, 154–157. https://doi.org/10.1038/nature01459
Yokoo, S., Hirose, K., Sinmyo, R. and Tagawa, S., 2019. Melting experiments on liquidus phase relations in the Fe-S-O ternary system under core pressures. Geophys. Rev. Lett., 46, 5137–5145. https://doi.org/10.1029/2019GL082277
Zurkowski, C.C., Lavina, B., Chariton, S., Tkachev, S., Prakapenka V.B. and Campbell A.J., 2022. The crystal structure of Fe_2S at 90 GPa based on single-crystal X-ray diffraction techniques. American Mineralogist: Journal of Earth and Planetary Materials, 107, 739 – 743. https://doi.org/10.2138/am-2022-7973
Zurkowski, C. C., Lavina, B., Brauser, N. M., Davis, A. H., Chariton, S., Tkachev, S., Greenberg, E., Prakapenka, V. B., and Campbell, A. J., *in press.* Pressure-induced *C*23-*C*37 transition and compression behavior of orthorhombic Fe_2S to Earth's core pressures and high temperatures. https://doi.org/10.2138/am-2022-8187